University of Wollongong

Research Online

Australian Institute for Innovative Materials - Papers

Australian Institute for Innovative Materials

1-1-2020

# On the Degradation of Retained Austenite in Transformation Induced Plasticity Steel

Ilana Timokhina

Azdiar Adil Gazder
*University of Wollongong*, azdiar@uow.edu.au

Jiangting Wang

Ilias Bikmukhametov

Peter Hodgson

*See next page for additional authors*

Follow this and additional works at: https://ro.uow.edu.au/aiimpapers

 Part of the Engineering Commons, and the Physical Sciences and Mathematics Commons

## Recommended Citation

Timokhina, Ilana; Gazder, Azdiar Adil; Wang, Jiangting; Bikmukhametov, Ilias; Hodgson, Peter; Niessen, Frank; and Pereloma, Elena V., "On the Degradation of Retained Austenite in Transformation Induced Plasticity Steel" (2020). *Australian Institute for Innovative Materials - Papers*. 4174.
https://ro.uow.edu.au/aiimpapers/4174

Research Online is the open access institutional repository for the University of Wollongong. For further information contact the UOW Library: research-pubs@uow.edu.au

# On the Degradation of Retained Austenite in Transformation Induced Plasticity Steel


## Abstract

© 2020, The Minerals, Metals & Materials Society and ASM International. A transformation-induced plasticity steel was thermomechanically processed and then transformed to bainite at an isothermal transformation temperature of 723 K for 1800 seconds, which exceeds the time required for completion of the bainite transformation. The formation of lenticular-shaped carbides with a triclinic lattice and internal substructure was found after thermomechanical processing. After 16 years of storage at room temperature, the decomposition of retained austenite into pearlite was observed for the first time at this temperature.



## Disciplines

Engineering | Physical Sciences and Mathematics

## Publication Details

Timokhina, I., Gazder, A., Wang, J., Bikmukhametov, I., Hodgson, P., Niessen, F. & Pereloma, E. (2020). On the Degradation of Retained Austenite in Transformation Induced Plasticity Steel. Metallurgical and Materials Transactions A: Physical Metallurgy and Materials Science,



## Authors

Ilana Timokhina, Azdiar Adil Gazder, Jiangting Wang, Ilias Bikmukhametov, Peter Hodgson, Frank Niessen, and Elena V. Pereloma



This journal article is available at Research Online: https://ro.uow.edu.au/aiimpapers/4174

# On the degradation of retained austenite in transformation induced plasticity steel.

Ilana B. Timokhina[a], Azdiar A. Gazder[b], Jiangting Wang[a], Ilias Bikmukhametov[ad], Peter D. Hodgson[a], Frank Niessen[b], Elena V. Pereloma[b,c]

[a]Institute for Frontier Materials, Deakin University, Geelong, VIC 3220, Australia

[b]Electron Microscopy Centre, University of Wollongong, Wollongong, NSW 2500, Australia

[c]School of Mechanical, Materials, Mechatronic and Biomedical Engineering, University of Wollongong, Wollongong, NSW 2522, Australia

[d]Department of Metallurgical & Materials Engineering, The University of Alabama, Tuscaloosa, Alabama, 35487, USA

ilana.timokhina@deakin.edu.au, azdiar@uow.edu.au, jiangting.wang@deakin.edu.au, ibikmukhametov@ua.edu, peter.hodgson@deakin.edu.au, contact@fniessen.com, elenap@uow.edu.au

*Corresponding author*: ilana.timokhina@deakin.edu.au

Abstract

A transformation-induced plasticity steel was thermo-mechanically processed and then transformed to bainite at an isothermal transformation temperature of 723 K for 1800s, which exceeds the time required for completion of the bainite transformation. The formation of lenticular-shape carbides with a triclinic lattice and internal substructure was found after thermomechanical processing. After 16 years storage at room temperature the decomposition of retained austenite into pearlite was observed for the first time at this temperature.

Keywords: transformation-induced plasticity steel; retained austenite decomposition; atom probe tomography; pearlite formation at room temperature; transmission electron microscopy; electron back-scattering diffraction.

## 1. Introduction

Retained austenite (RA) is an important phase in many modern advanced high strength steels, such as Transformation-Induced Plasticity (TRIP) steels [1-5], nanobainitic steels [6-8], quenched and partitioned (Q&P) steels [9-12] and medium-Mn steels [13-15]. In all of these steel grades, RA is the product of an incomplete bainite transformation due to the high Si concentration leading to the high carbon content of RA [16, 17]. To a large extent, the carbon and manganese contents of the RA determine its chemical stability [1, 18, 19]. The microstructure and stability of the RA is important for production and in-service performance of components manufactured from the steel, as any changes in the microstructure (phase constituents, morphology, coarseness, etc.) have a direct effect on the mechanical properties (toughness, yield strength, crashworthiness, etc.). A high carbon concentration in the RA is desirable as it promotes stability on cooling and against the deformation-induced martensite transformation [18, 19]. However, this also makes the RA more susceptible to decomposition into ferrite and carbides at elevated temperatures due to the increased driving force for carbides precipitation from austenite with higher carbon content [20]. The precipitation of carbides in bainite during early stages of the bainite transformation also leads to less stable RA and its transformation to martensite on subsequent cooling [21-23]. The stability of the RA is also somewhat related to its morphology, as it has been commonly reported that film-like RA between neighbouring subunits of bainitic ferrite (BF) has a higher carbon content compared to the blocky RA located between sheaves of bainite [20, 24]. However, it was recently shown that blocky RA could have a high carbon content similar to film RA [25].

With the progress of the incomplete bainite transformation, the carbon enrichment of the RA increases until a critical level, at which the RA decomposition takes place. For example, this occurs when the holding time at isothermal transformation temperature exceeds the time required for the bainitic reaction [17]. Alternatively, for the same holding time, an increase in the isothermal bainite transformation temperature/tempering temperature will have a similar effect on the carbon content in the RA and result in accelerated RA decomposition [26, 27].

To-date, there is limited information available with respect to the mechanism of RA decomposition and on the types of carbides formed. Park et al. [26] reported that no decomposition of the RA was observed in a Fe-0.2C-2.Mn-1Si-1Al (wt.%) TRIP steel after tempering at temperatures below 473K. However, at higher temperatures, the first precipitate to form in partially decomposed RA was ε-carbide followed by the precipitation of cementite. The latter became globular and spheroidised at longer holding times at high temperatures. On the other hand, in a medium Mn steel (Fe-0.1C-5Mn wt.%) the RA decomposition was delayed to temperatures above 673 K; blocky RA decomposed into ferrite and rod-like cementite at 723 K. Similarly, the formation of cementite was only detected after tempering for 30 min or longer at 723K for a Fe-0.2C-3Mn-2Si wt.% steel [23]. Full decomposition of the RA into ferrite and cementite was observed in both TRIP and nanobainitic steels after reheating and holding for 3 hrs at 723K [28]. Atom probe study of hot-worked tool steel showed a laminar arrangement of cementite after RA decomposition at 883K [22]. Another morphology of carbide formed on the decomposition of RA has been reported by Sandvik [29] in a 0.9C-2Si-0.5Mn-0.42Cr wt.% steel at 653 K , with ~100nm thick, lenticular plate-shaped carbides with a triclinic crystal lattice and a midrib.

To the best of the authors' knowledge, there have not been any studies to-date on RA stability during long term service life at ambient temperatures. In this work, this deficiency is addressed by studying the microstructure of thermo-mechanically processed TRIP steel [30] after more than 16 years in storage using a combination of transmission electron microscopy (TEM), electron back-scattering diffraction (EBSD), and atom probe tomography (APT).

## 2. Material and Methods

The nominal composition of the TRIP steel used in this study was Fe-0.21C-1.51Mn-1.49Si- 0.004Mo - 0.01Al - 0.036Nb wt.%.Thermo-mechanical processing (TMP) was

undertaken on a laboratory rolling mill. The TMP schedule (Fig. 1) was constructed by utilising continuous-cooling-transformation data [31]. The strip was reheated in a 15 kW muffle furnace and soaked at 1523 K for 120 s. After soaking, the strip was 25% rough rolled at 1373 K followed by a 120s hold to uniformly condition the recrystallised austenite. Subsequent 47% finish rolling in the non-recrystallised region was undertaken at 1123 K followed by cooling at 1 $K \cdot s^{-1}$ to the accelerated cooling start temperature of 943 K to form ~50 vol.% of polygonal ferrite; which is the optimal amount required to stabilise the highest volume fraction of RA [32]. Following this, two spray guns were used to cool the strip at ~20 K/s to 773 K to avoid pearlite formation. At this point, coiling was simulated by lowering the strip into a fluid bed furnace, covering it with aluminium oxide sand and isothermally holding at 723 K for 1800 s to form bainite. Following this, the strip was quenched in an iced brine solution (Fig. 1). The final strip thickness was ~6.5 mm. The strip was produced in 2002 and kept in storage at room temperature (RT) for 16 years. This enables study of the effect of prolonged storage on the TRIP steel microstructure.

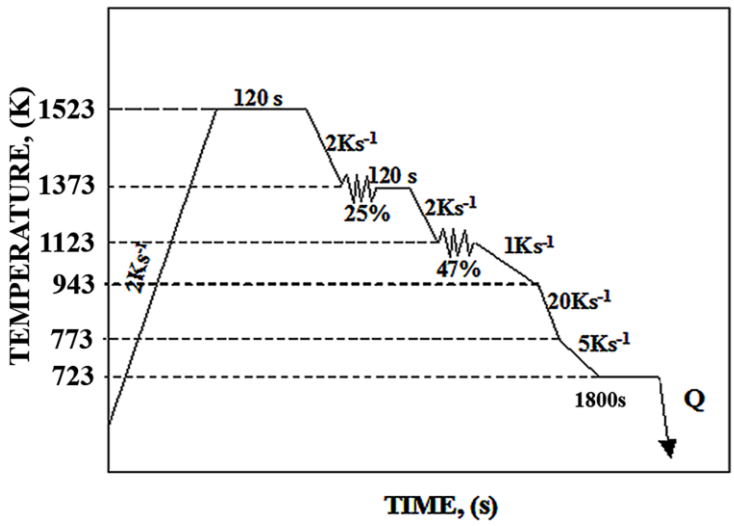


Figure 1. Thermomechanical processing schedule.

The volume fraction of RA was measured using a Philips PW 1130 diffractometer equipped with a Ni-monochromated Cu Kα radiation source operated at 40 keV and 25 mA in Bragg-Brentano geometry. The relative intensities of the peaks were recorded by varying 2θ from 40°-90° in

111 continuous scan mode at a rate of 0.5° $min^{-1}$ with a step size of 0.05°. The volume fraction of RA
112 was estimated by the direct comparison method using the integrated intensities of the $(200)_\alpha$
113 and $(211)_\alpha$ peaks from bcc ferrite and the $(200)_\gamma$ and $(220)_\gamma$ peaks from fcc austenite [33].
114 Since the original strip was produced in 2002, electron backscattering diffraction (EBSD) maps
115 of the microstructure after TMP was not carried out as this technique was not accessible at that
116 time. However, the strip subjected to prolonged room temperature storage for 16 years, was
117 mapped.
118 The samples for EBSD were cut from the centre of the aged strip width along the normal
119 direction–rolling direction (ND–RD) and mechanically ground to 0.3 mm thickness using up to
120 1200 grit silicon carbide paper. Ø3 mm discs were punched out, after ensuring that each disc
121 contained a short chord parallel to the RD, in order to identify the macroscopic sample
122 coordinates. The discs were manually ground to ~70 μm thickness using 2400 and 4000 grit
123 silicon carbide papers, and then twin-jet electro-polished to produce electron transparent foils
124 using a solution of 90% methanol and 10% perchloric acid in a Struers Tenupol-5 operated at
125 30 V, ~150 mA and 243 K.
126 EBSD orientation and Energy Dispersive Spectroscopy (EDS) elemental data were obtained
127 simultaneously from the centre of the ND–RD cross- section using a JEOL JSM-7001F field
128 emission gun scanning electron microscope operated at 15 kV accelerating voltage, ~5.1 nA
129 probe current, 12 mm working distance at ×1000 magnification. The microscope was fitted with
130 a Nordlys-II(S) EBSD detector and an 80 $mm^2$ X-Max EDS detector interfacing with the Oxford
131 Instruments (OI) Aztec software suite. A step size of 0.06 μm was employed such that a map
132 comprising 2000 × 1500 pixels, which corresponds to an area of 20 × 90 $\mu m^2$, was collected
133 over ~61.5 hours.
134 The EBSD mapping conditions were optimised beforehand with a 16.33 ms camera exposure
135 time, 43 and 32 reflectors employed for the bcc and fcc phases, respectively, 4×4 binning, 3
136 background frames, a Hough resolution of 60. The speed of acquisition of the individual electron
137 backscattering patterns was 13.5 Hz (~73.9 ms) with up to 11 Kikuchi bands concurrently

indexed via the OI “Refined Accuracy” algorithm. The raw EBSD maps returned an overall indexing rate of 97.48% such that most of the zero solutions were concentrated at boundary interfaces.

EDS maps were obtained using a 0-20 keV energy range, 2048 channels, a process time of 3, a detector dead time of 50–55% and a pixel dwell time of 24.8 ms. Over the full ‘TruMap’ area, the Fe-K, Mn-K, Si-K, C-K, Nb-L, Cu-L, Al-K and Mo-L lines returned distributions of relative frequency versus counts per second (cps) with maximum counts rounded-off to 1055, 232, 335, 225, 119, 57, 670 and 695, respectively.

Post-processing of the EBSD maps were undertaken using the Oxford Instruments HKL Channel-5 software suite. In brief, it involved the removal of wild spikes and cyclic extrapolation of zero solutions up to five neighbours followed by thresholding the band contrast histogram to delineate unindexable regions (Fig. 2a). Since the EBSD maps were indexed as iron fcc (austenite) and bcc (ferrite) during acquisition, a previously developed procedure using the OI Channel-5 software suite [34] was modified to initially segment the phases into austenite, polygonal ferrite, and an unsegmented fraction comprising bainite, a mixed region of martensite/pearlite and carbides. While a detailed step-by-step guide to segment polygonal ferrite from the unsegmented fraction is given in Ref. [34], a brief description of the procedure to segment bainite and the mixed region of martensite/pearlite and carbides is as follows.

To segment the bainite and the mixed region of martensite/pearlite and carbides, the C-K EDS map data of that subset was imported as an *.tiff image into the Ilastik v3.1 software. Ilastik is an open source software for image classification and segmentation [35]. Using the in-built, machine learning pixel classification algorithms, the subset was segmented into an image comprising three grayscale colour thresholds for bainite, the mixed region of martensite/pearlite and carbides signifying lower, medium and highest carbon contents, respectively (Fig. 2b last carbon-K map). A specifically written MATLAB script read and assigned the varying grayscale colours to individual pixels of the *.ctf file. Following this, the *.ctf file was re-imported back into OI

Channel-5 and the varying grayscale colours assigned as separate phases; in order to colour-code the phase map (Fig. 2c phase map).

Bright field (BF), dark field (DF) and selected area electron diffraction (SAED) studies were undertaken on a Philips CM20, operated at 200 kV to characterise the initial microstructure after TMP in 2002. Similar work was performed to study the strip after 16-year storage using a JEOL 2100F operated at 200 kV. In both cases, electron transparent thin foils were prepared by twin-jet electro-polishing. Orientation distributions along BF layers were studied by SAED patterns using an aperture of 1.1 μm nominal diameter.

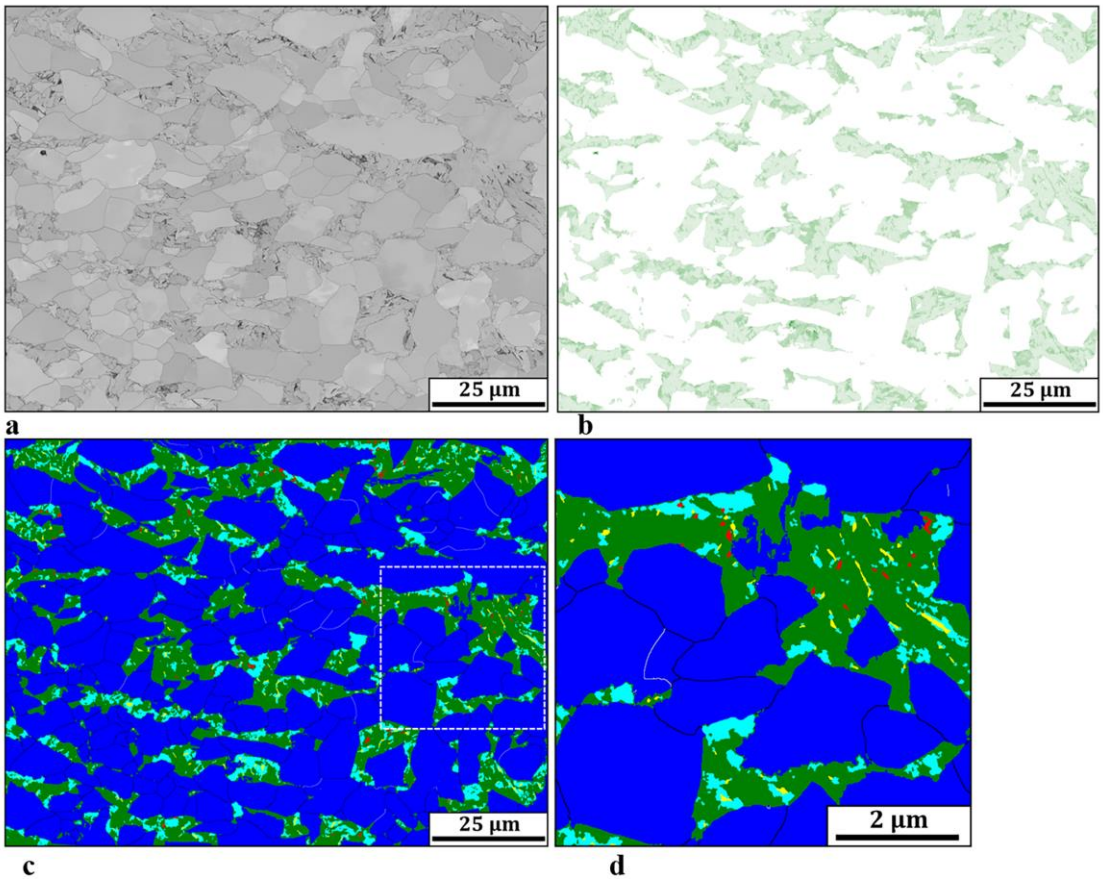


Figure 2. Representative (a) band contrast, (b) carbon – K and (c) phase maps. In (b), the areas exclude polygonal ferrite and austenite. The area denoted by the white dashed rectangle in (c) is magnified in (d). In (c) and (d) red = austenite; blue = polygonal ferrite; green = ferrite in bainite; yellow = carbides; aqua = mixed region (see text for details).

Atom probe tomography (APT) was used to study the variation in local chemical composition of the phases, solute redistribution and segregation across the phases [36]. APT needles were prepared from bulk polished sample and TEM foils using focused ion beam milling (FIB) in a dual beam FEG-SEM (FEI Quanta 3D). For example, pearlitic regions were identified and their location marked on the foil using TEM (Fig. 3). Following this, Pt supporting layers were deposited in the region of interest on both sides of the foil (Fig. 3b). The targeted specimens were then cut from the region of interest and lifted out on to an APT sample holder. Finally, APT needles were sharpened using the FIB operated at 30 kV for initial shaping and 8 kV for final polishing.

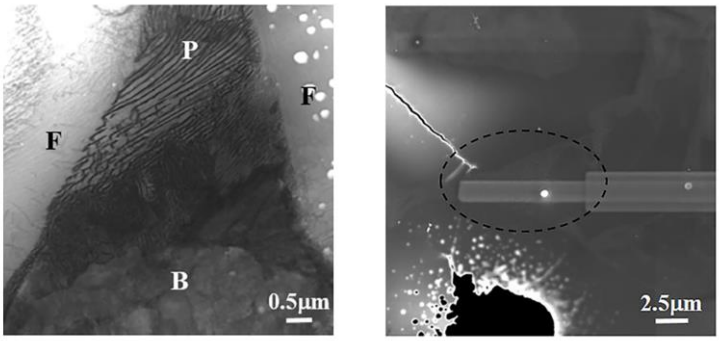


Figure 3. TEM micrograph (a) and position of APT sample (b) taken from pearlite shown in (a). F is ferrite, P is pearlite, B is bainite. Dash line outlines the pearlite region and APT sample taken from this area.

APT was conducted on a Cameca LEAP 5000 XR operated in voltage mode with a pulse rate of 200 kHz and a sample temperature of 60 K. Data reconstruction and quantitative analysis was undertaken within the IVAS 3.6.14 software suite [36]. Phase composition was determined from the regions without visible coarse particles, boundaries and/or defects.

Thermodynamic modelling was applied to assess the phase equilibrium for the local composition of RA at ambient temperature. The calculations were performed with Thermo-Calc 2020a [37] using the TCFE9 thermodynamics database [38].

## 3. Results

The microstructure after TMP comprised ~50% of polygonal ferrite with layers of granular bainite and acicular ferrite (Fig. 4a). RA islands and films were located in-between polygonal ferrite grains, at interfaces between polygonal ferrite and BF, between BF laths and as martensite/RA constituent (Fig. 4). XRD confirmed that the steel contained ~5% RA. In addition, coarse, lenticular-shaped carbides (hereafter referred to as LSC) were detected in bainite between the BF laths (Fig. 4b). The morphology of LSC differed significantly from those seen previously in upper and lower bainite [17, 31] and they also contained a high density of internal faults (Figs. 4b-4d). The average size of LSC was estimated using their projected lengths in the $(111)_{\alpha}$ matrix plane such that they averaged 370±100 nm length and 100±30 nm width. Indexing their diffraction patterns showed that the LSC crystal structure was close to triclinic (or alternatively, distorted orthorhombic) with approximate lattice parameters of a = 0.638 nm, b = 0.505 nm, c = 0.459 nm, and α = 90°, β = 70.1° and γ = 84.7° [29]. In some cases, TEM also revealed the presence of LSC near RA; an observation that could be ascribed to the partial decomposition of RA that leads to the formation of LSC and ferrite (Figs. 4c and 4d). TEM investigation showed that "recovered ferrite", or ferrite grains with dislocation density lower than that in BF but a higher than in PF (for example, the area marked by F in Fig. 4c), are present in the areas in close proximity to LSC, presumably as a result of the decomposition of RA.

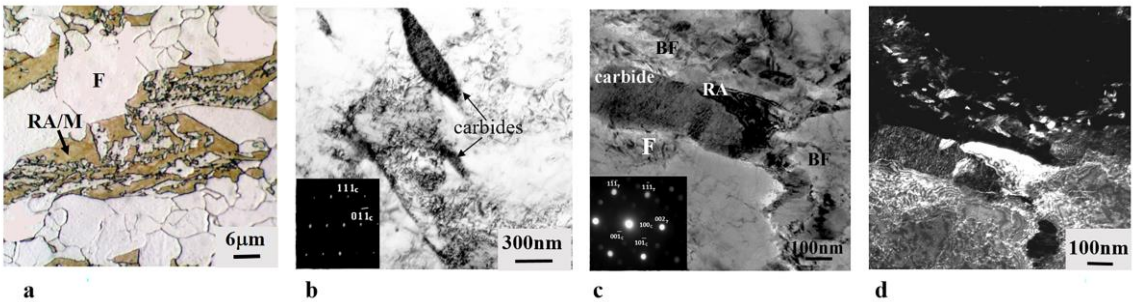

Figure 4. Optical micrograph (a), TEM bright field (b, c) and TEM dark field from (002)γ diffraction spot (d) micrographs showing initial microstructure of TRIP steel after 1800 s isothermal hold at 723K (a), lenticular carbides (b) and decomposed austenite (c, d) in the samples after TMP. Zone axis for (b) is $[2\bar{1}\bar{1}]$, and for (c) is $[110]_\gamma$ // $[010]_c$.

SEM on bulk samples (Fig. 5a) together with EBSD (Fig. 2) and TEM (Fig. 6) after 16 years room-temperature storage confirmed the following microstructural features: (i) the formation of lamella-like, coarse pearlite between ferrite grains (Figs. 5, 6c), (ii) lamella-like, fine or degenerate pearlite formed at the ferrite/bainite interface, (Figs. 2c, 2d, 6a, 6b) and (iii) the presence of LSC in bainite (Figs. 2d and 6d).

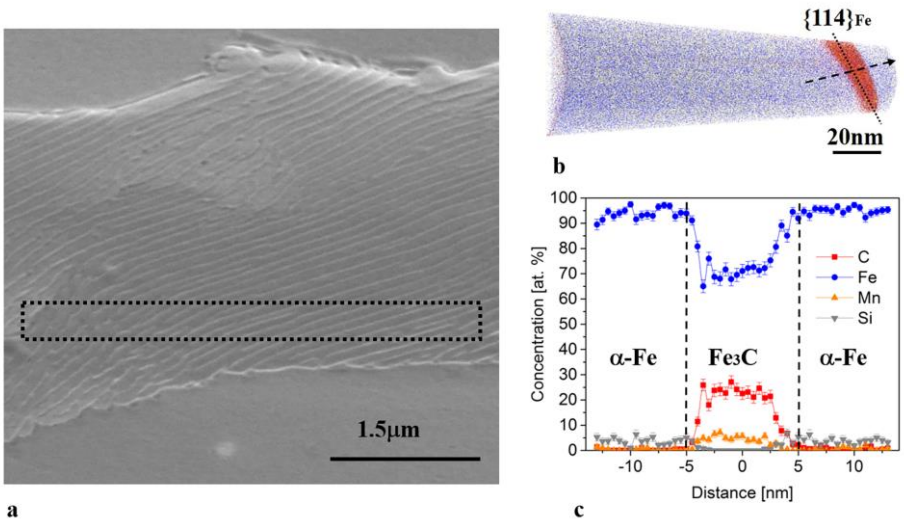


Figure 5. SEM micrograph showing position of APT sample (dash line) taken from pearlite (a), corresponding Fe-C atom map (b) and composition profile across cementite in pearlite (along dash line shown in atom map (b)) (c).

In the representative phase map shown in Fig. 2c, austenite, polygonal ferrite, ferrite in bainite and carbides are denoted by red, blue, green and yellow colours which correspond to map areas of 0.18%, 69.4%, 23.5% and 0.49%, respectively. The yellow areas (Figs. 2c and 2d) possess the

highest carbon content (Fig. 2b) and their morphology correlates with the LSC seen in TEM (Fig. 6d). The 6.43% area denoted by the aqua colour comprises the mixed region of martensite, pearlite or secondary formed ferrite via RA decomposition. It is also noted that the aqua areas in the immediate vicinity of a carbide could be a diffusion zone of carbon enrichment; in which case these localised regions could also be carbon enriched BF.

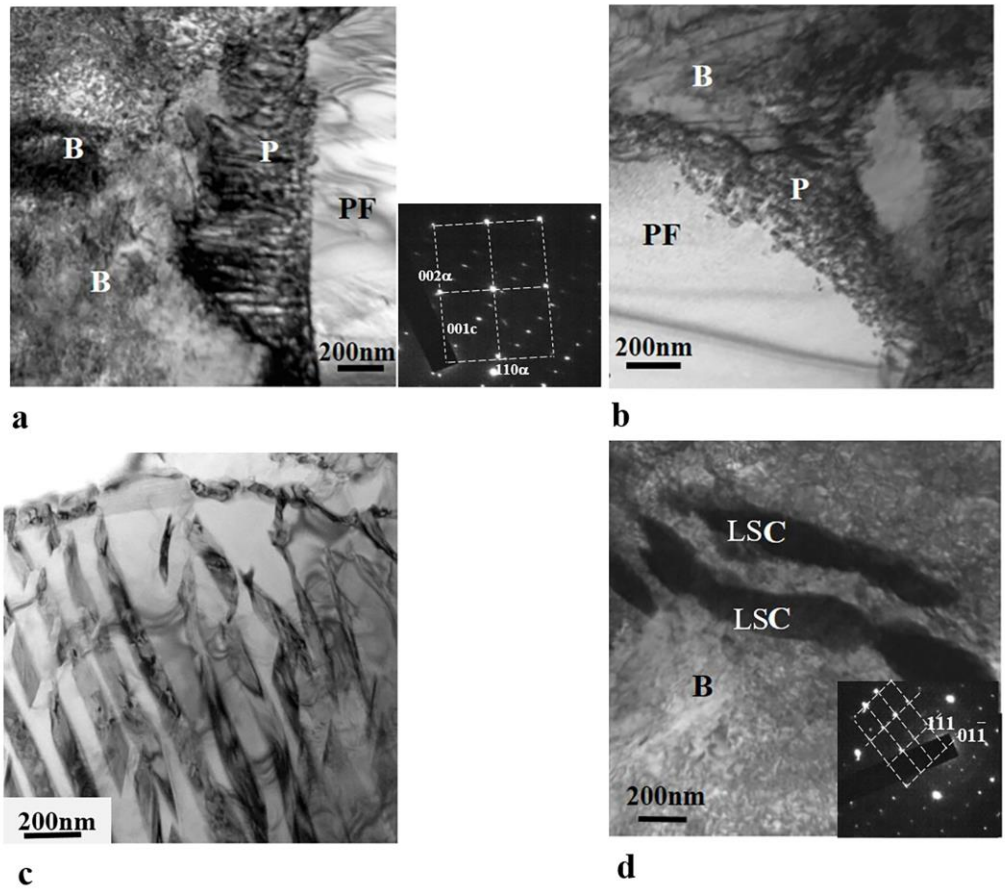


Figure 6. Representative TEM micrographs of the microstructure after 16 years in storage: (a) lamella-like ([1-10]a//[-100]c and (b) degenerate pearlite, (c) pearlite in ferrite and (d) presence of LSP in bainite (zone axis is [-2-11]). PF is polygonal ferrite, B is bainite, P is pearlite and LSC is lenticular shape carbides. Note that coarse pearlite is not edge-on in (c) in order to better reveal the cementite layers.

Two types of pearlite with different inter-lamellar distances were observed: (i) coarse and (ii) fine. The thickness of cementite layers in coarse pearlite was 12±3 nm, while the thickness of ferrite was 100±10 nm (Fig. 5). In the case of fine pearlite (Figs. 6a, and 7), the thickness of cementite was ~10 ±2 nm and the thickness of ferrite was ~ 50±5 nm.

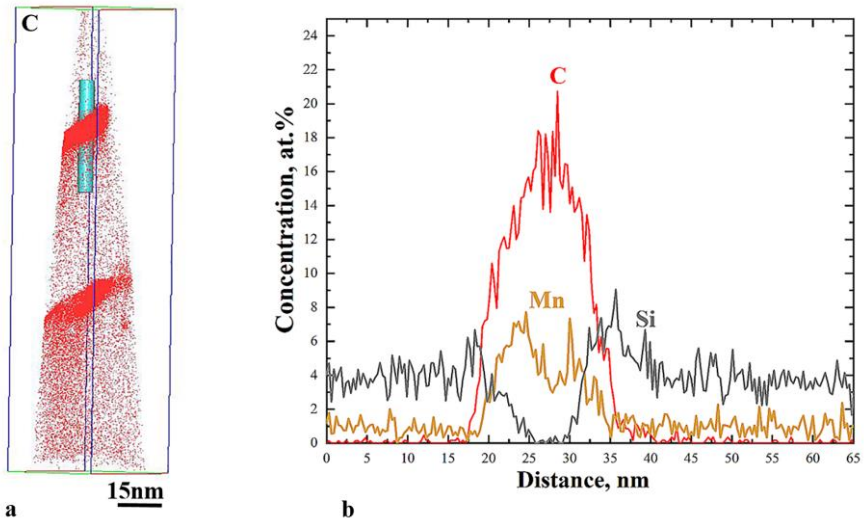


Figure 7. Representative carbon atom map (a) and concentration profile (b) along the box shown in (a) of pearlite from the site specific sample shown in Figure 3.

The carbon atom maps from the site-specific APT needles proved the formation of cementite and ferrite lamellae (Figs. 5b, 5c and 7a). The average cementite and ferrite thicknesses were comparable to that obtained from SEM and TEM data for both coarse and fine pearlite. The average carbon content calculated from the centre of these cementite layers varied from 18 to 27 at.%; which correlates well with its expected ~25 at.% carbon content (Figs. 5c, 7b). The 1D concentration profiles also showed: (i) the partitioning of Mn to cementite (increasing from 1.5 at.% in ferrite to ~6 at.% within the cementite layers) and, (ii) the depletion of Si in cementite layers to ~0.01 at.% compared to ~3.8 at.% in ferrite (Figures 5c and 7b).

Based on APT, it was found that prolonged storage for 16 years affected the redistribution of solutes, mainly carbon, between and within the phases. This occurred in BF and RA/martensite

due the high dislocation densities of these phases. Firstly, segregation of C and Mn at ferrite/bainite interfaces was observed (Fig. 8a).

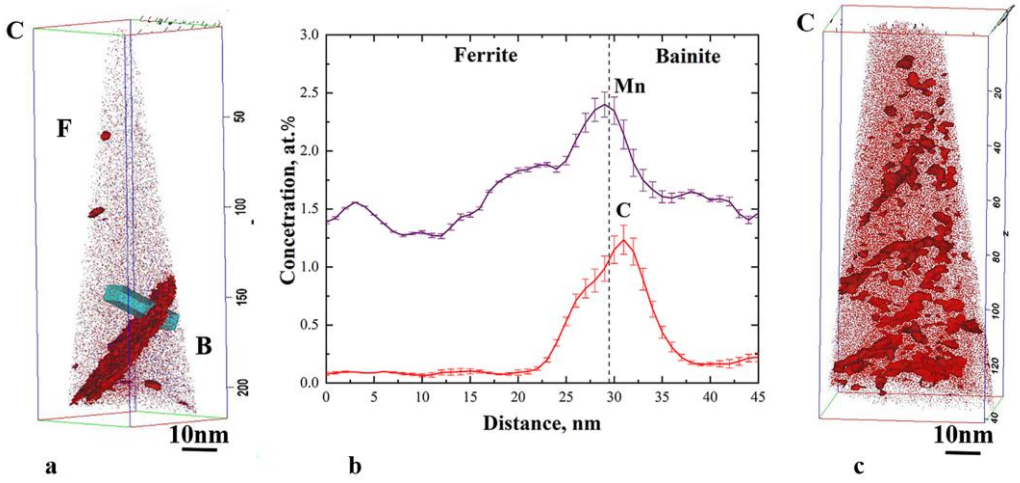


Figure 8. Representative carbon atom map (a, c) and concentration profile (along the box shown in (a)) across ferrite/bainite interface (b); and segregation of C at dislocations in martensite/retained austenite (5 at.%C iso-surface ) (c). F is ferrite and B is bainite.

The local concentration profile along the selected box perpendicular to a ferrite/bainite interface shows an increase in C level from ~ 0.06 ± 0.01 at.% in the matrix of polygonal ferrite to 1.2 at.% at the interface. At the same time, the BF continued to be saturated in carbon (~0.2 ± 0.02 at.%). The Mn level is 2.4 at.% at the interface and it gradually decreases to ~ 1.38 ± 0.1 at.% in the matrix of polygonal ferrite and to ~ 1.56 ± 0.08 at.% in BF (Figs. 8a, 8b). Secondly, a carbon segregation at dislocations and the formation of carbon clusters in martensite/RA were also found in this condition. (Fig. 8c).

## 4. Discussion

Since maintaining the required level of the RA stability is necessary for TRIP steel sustainability, it is important to study the microstructural changes after prolonged room temperature exposure.

In this regard, the addition of Si to this TRIP steel is important as it typically inhibits the formation of cementite; a process that removes carbon from RA. It follows that inhibiting cementite formation is crucial to the overall stability of RA which increases with the progress of the bainite transformation [39]. However, if the coiling time exceeds the time of the bainite reaction, then the RA can decompose with the formation of secondary ferrite and carbides [29].

The TEM investigation revealed the presence of LSC within bainite after isothermal holding for 1800 s. The morphology of these LSC is dissimilar to ε-carbides or cementite that precipitate rapidly in upper or lower bainite [17]. It also differs from the thin carbide needles formed in BF laths observed after 40 min holding at 773 K in a 1.83Si wt.% steel [40] such that their formation was ascribed to the secondary stage of the bainite reaction. As these LSC were not a representative feature in the TMP steel with a shorter (600s) holding time at 723 K (please see Refs. [31, 32] by the same co-authors), and bainite formation was completed in that condition, it could be suggested that the LSC formed by decomposition of residual austenite that was highly-enriched in carbon (4-7at.%). Previous APT studies of RA in TRIP steels after TMP [25, 31] indicate a wide range of carbon contents depending on its size, location and neighbouring phases as well as the inhomogeneous distribution of carbon within RA. Thus, prolonged exposure at 723 K enables carbon to continue diffusing from supersaturated BF into RA. Consequently, regions close to BF are enriched in carbon; which triggers the formation of LSC in thin RA layers between BF laths (Fig. 4b) or in part of a coarser RA (Fig. 4c). The part of the RA that is less enriched in C remains stable on cooling to room temperature. These LSC closely resemble the carbides observed by Sandvik [29] where LSC demonstrated extensive faulting and lenticularity and their crystal structure was identified as triclinic or distorted orthorhombic. All of these factors support the hypothesis proposed by Sandvik [29] that the

356 formation of such carbides takes place during the decomposition of RA by the shear mechanism.
357 Here it should be noted that a phase forming by a diffusion-controlled mechanism is expected to
358 contain a comparatively lower density of faults [29]. Moreover, it was also suggested by Sandvik
359 [29] that the high density of internal defects in the LSC could be inherited from the stress
360 accumulation in RA that is associated with BF formation.

361 Based on the above considerations, a proposal for the kinetics of the transformation events
362 occurring during the isothermal holding time is proposed. The nucleation of BF immediately
363 followed by the initiation of its growth, begins the process of carbon partitioning into residual
364 austenite. Since the distribution of carbon is inhomogeneous within and between differently
365 sized morphologies of RA, this phase could possess low, intermediate and supersaturated levels
366 of carbon. In turn, this leads to the RA behaving differently with increased isothermal holding
367 time. Here, the RA with the lowest carbon content easily transforms to martensite during
368 quenching whereas the RA with an intermediate carbon content remains stable at room
369 temperature. It follows then that the RA supersaturated with carbon decomposes, probably by
370 the shear mechanism, to form LSC and secondary ferrite.

371 In this case, the effect of increasing the isothermal holding time during coiling can be
372 summarized as having two effects. (i) It leads to an increase in the fraction of supersaturated
373 RA, which decomposes easily during subsequent holding. (ii) Alternatively, it increases the
374 overall stability of low carbon RA, which, in turn, inhibits martensite formation during
375 quenching.

376 The hypothesis that RA contains varying carbon content is strengthened by TEM investigations
377 of the samples after prolonged room-temperature storage. Imaging revealed the presence of
378 pearlite at BF/polygonal ferrite interfaces or in-between polygonal ferrite grains (Figs. 5a and 6
379 a-c). However, the EBSD map (Fig. 3c) revealed that not all of the RA decomposed into pearlite,
380 which also indicates the inhomogeneity in carbon content between and within the RA crystals. It
381 is interesting to note that if the area percentages of the red (0.18%) and aqua (6.43%) regions

are summed, the resulting 6.61% area fraction is similar to the original RA fraction estimated by XRD after TMP. The decomposition of RA following the initial rapid formation of BF has only been studied at elevated temperatures [23, 26, 28, 29]. The possibility of RA decomposing into thermodynamically stable ferrite and carbides at room temperature has not been reported to date.

Due to the high rate of carbon diffusion, even at RT, carbon atoms will continue re-arranging with the formation of clusters and Cottrell atmospheres at dislocations in BF (Fig. 8c) competing with carbon diffusion to RA where carbon has higher solubility compared to BF. Since APT studies after TMP showed that carbon content in RA typically exceeds 3 at.% and can be as high as 7 at.%, and taking into account that these values could have been increased during several years at RT, equilibrium calculations were conducted in Thermo-Calc to assess the thermodynamic driving force for pearlite formation from RA, $\Delta G_{pearlite}$, which is defined as:

$$\Delta G_{pearlite} = G_{ferrite} + G_{cementite} - G_{austenite} \quad (1)$$

with $G$ being the Gibbs energy of the phases. The values for $G_{ferrite}$ and $G_{cementite}$ are under the assumption that cementite and ferrite partition in para-equilibrium, i.e. only by diffusion of the interstitial element C. The calculation was conducted on the intermediate composition of RA Fe-4.80C-1.06Mn-1.40Si at.%. Fig. 9 shows the molar driving force for pearlite formation from RA as a function of temperature with a step size of 50 K. Driving force and temperature show an inversely proportional relationship in which the driving force increases from 1.0 to 5.5 kJ/mol during cooling in the 500 K temperature interval. The computed driving force supports that the transformation at low temperature is definitely thermodynamically feasible. The pearlite property model in Thermo-Calc [41] was used to attempt an assessment of the experimentally-observed pearlite formation kinetics. However, since hardly any experimental data on C boundary diffusivity and interfacial mobility is available below 800 K, the calibration of the model was optimized for the temperature range 800 – 1000 K. Thus, predictions of the kinetics

of pearlite formation at room-temperature require too much of an extrapolation and are not reliable.

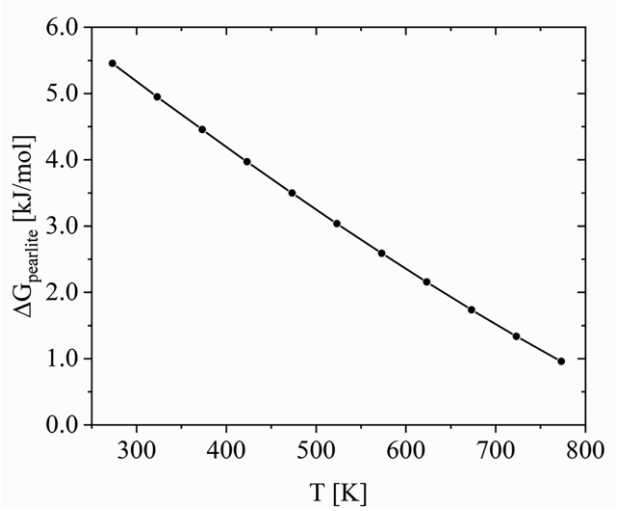


Figure 9. Molar driving force for pearlite formation, $\Delta G_{pearlite}$, from the intermediate composition of retained austenite under the assumption of para-equilibrium between ferrite and cementite as a function of temperature.

## 5. Conclusions

Lenticular shape carbides with high density of internal defects were found after isothermal holding for 1800 s and after 16 years storage at room temperature. It was suggested that the carbides were formed as a result of decomposition of residual austenite. This austenite is located in close proximity to BF and enriched in carbon. Partial RA decomposition with pearlite formation was observed in TRIP steel after 16 years storage at room temperature. This supports the inhomogeneity in the distribution of carbon within and between RA grains based on their morphology and location in a TMP TRIP steel. Furthermore, it posed the question regarding the longtime RA stability under service conditions and its effect on component properties. Thermo-Calc calculations support the feasibility of pearlite formation from the RA due to a high thermodynamic driving force for its formation.

## Acknowledgements

The authors would like to acknowledge the financial support of Deakin University and the University of Wollongong, Australia. Deakin University's Advanced Characterisation Facility is acknowledged for use of the FIB-SEM, TEM, and APT. The JEOL JSM-7001F at the UOW-EMC was funded by the Australian Research Council – Linkage, Infrastructure, Equipment and Facilities grant LE0882613. The Oxford Instruments 80 $mm^2$ X-Max EDS detector was funded via the 2012 UOW Major Equipment Grant scheme. A. Gazder acknowledges the 2019 AIIM for Gold - Investigator grant.

## References

[1] B.C. De Cooman, *Curr. Opin. Solid State Mater. Sci.*, 2004, vol. 8(3–4), pp. 285-303.
[2] P.J. Jacques, *Curr. Opin. Solid State Mater. Sci.*, 2004, vol. 8, pp. 259-265.
[3] O. Matsumura, Y. Sakuma, H. Takechi, *Scripta Metall.*, 1987, vol. 21, pp. 1301-1306.
[4] I.B. Timokhina, P.D. Hodgson, E.V. Pereloma, *Metall. Mater. Trans. A,* 2004, vol. 35A(8), pp. 2331-2341.
[5] E. Pereloma, H. Beladi, L. Zhang, I. Timokhina, *Metall. Mater. Trans. A,* 2012, vol. 43A, pp. 3958-3971.
[6] F.G. Caballero, H.K.D.H. Bhadeshia, K.J.A. Mawella, D.J. Jones, P. Brown, *Mater. Sci. Technol.*, 2002, vol. 18(3), pp. 279-284.
[7] F.G. Caballero, H.K.D.H. Bhadeshia, *Curr. Opin. Solid State Mater. Sci.*, 2004, vol. 8(3), pp. 251-257.
[8] F. Caballero, C. Garcia-Mateo, M. Miller, *Mater. Sci. Technol.*, 2015, vol. 31, pp. 764-772.
[9] J. Speer, D.K. Matlock, B.C. De Cooman, J.G. Schroth, *Acta Mater.,* 2003, vol. 51(9), pp. 2611-2622.
[10] D.V. Edmonds, K. He, F.C. Rizzo, B.C. De Cooman, D.K. Matlock, J.G. Speer, *Mater. Sci. Eng. A,* 2006, vol. 438-440, pp. 25-34.
[11] L. Liu, B. He, G.-J. Cheng, H.-W. Yen, M.X. Huang, *Scr. Mater.* 2018, vol. 150, pp. 1-6.
[12] X. Tan, D. Ponge, W. Lu, Y. Xu, X. Yang, X. Rao, D. Wu, D. Raabe, *Acta Mater.*, 2019, vol. 165, pp. 561-576.
[13] T. Furukawa, H. Huang, O. Matsumura, *Mater. Sci. Technol*., 1994, vol. 10, pp. 964-970.
[14] D.W. Suh, J.H. Ryu, M.S. Joo, H.S. Yang, K. Lee, H.K.D.H. Bhadeshia, *Metall. Mater. Trans. A*, 2013, vol. 44A, pp. 286-293.
[15] Y.-K. Lee, J. Han, *Mater. Sci. Technol.,* 2015, vol. 31(7), pp. 834-856.
[16] H.K.D.H. Bhadeshia, D. Edmonds, *Metall. Trans. A*, 1979, vol. 10, pp. 895-907.
[17] H.K.D.H. Bhadeshia, *Bainite in Steels: Transformations, Microstructure and Properties*, Second ed. ed., Institute of Materials, Minerals and Mining, London, 2001.
[18] E. Pereloma, A.A. Gazder, I. Timokhina, *Retained austenite: transformation-induced plasticity*, in: R. Colas, G.E. Totten (Eds.) Encyclopedia of Iron, Steel, and Their Alloys, CRC Press, New York, 2016, pp. 3088-3103.
[19] E. De Moor, D.K. Matlock, J.G. Speer, M.J. Merwin, *Scr. Mater.,*2011, vol. 64(2), pp. 185-188.

[20] A.S. Podder, I. Lonardelli, A. Molinari, H.K.D.H. Bhadeshia, *Proc. R. Soc. A*, 2011, vol. 467, pp. 3141-3156.
[21] W. Shi, L. Li, B.C. De Cooman, P. Wollants, C.-X. Yang, *J. Iron Steel Res. Int.*, 2008, vol. 15, pp. 61-64.
[22] C. Lerchbacher, S. Zinner, H. Leitner, *Mater. Sci. Eng. A,* 2013, vol. 564, pp. 163 - 168.
[23] A.S. Podder, H.K.D.H. Bhadeshia, *Mater. Sci. Eng. A*, 2010, vol. 527(7), pp. 2121 - 2128.
[24] C. Garcia-Mateo, F.G. Caballero, M.K. Miller, J.A. Jimenez, *J. Mater. Sci.*, 2012, vol. 47(2) pp. 1004-1010.
[25] Z.P. Xiong, A.A. Saleh, R.K.W. Marceau, A.S. Taylor, N.E. Stanford, A.G. Kostryzhev, E.V. Pereloma, *Acta Mater.*, 2017, vol. 134, pp. 1 - 15.
[26] H.-S. Park, J.-B. Seol, N.-S. Lim, S.-I. Kim, C.-G. Park, *Mater. Des.*, 2015, vol. 82, pp. 173 - 180.
[27] Y.K. Lee, H.C. Shin, Y.C. Jang, S.H. Kim, C.S. Choi, *Scr. Mater.*, 2002, vol. 47(12), pp. 805 - 809.
[28] F.G. Caballero, C. Garcia-Mateo, C. Garcia de Andres, *Metall. Trans. A,* 2005, vol. 46(3), pp. 581-586.
[29] B.P.J. Sandvik, *MTA*, 1982, vol. 13(5), pp. 777-787.
[30] I.B. Timokhina, P.D. Hodgson, E.V. Pereloma, in: E.F. Palmiere, M. Mahfouf, C. Pinna (Eds.) International Conference on Thermomechanical Processing: Mechanics, Microstructure & Control, Sheffield University, UK, 2003, pp. 115-121.
[31] E.V. Pereloma, I.B. Timokhina, M.K. Miller, P.D. Hodgson, *Acta Mater.*, 2007, vol. 55(8), pp. 2587-2598.
[32] I.B. Timokhina, E.V. Pereloma, P.D. Hodgson, *Mater. Sci. Technol.*, 2001, vol. 17(2), pp. 135-140.
[33] B.D. Cullity, *Elements of x-ray diffraction*, Addison-Wesley Publishing Company, Inc., Reading, MA, 1978.
[34] A.A. Gazder, F. Al-Harbi, H.T. Spanke, D.R.G. Mitchell, E.V. Pereloma, *Ultramicroscopy*, 2014, vol. 147, pp. 114-132.
[35] C. Sommer, C. Straehle, U. Koethe, F.A. Hamprecht, Ilastik: Interactive Learning and Segmentation Toolkit, IEEE International Symposium on Biomedical Imaging, doi:10.1109/ISBI.2011.5872394. ISBN 978-1-4244-4127-3, 2011, pp. 230–33.
[36] M.K. Miller, R.G. Forbes, *Atom-Probe Tomography: The Local Electro Atom Probe*, Springer, New York, 2014.
[37] J.O. Andersson, T. Helander, L. Höglund, P. Shi, B. Sundman, *Calphad*, 2002, vol. 26(2), pp. 273-312.
[38] Y. Hirotsu, S. Nagakura, *Acta Metall.*, 1972, vol. 20(4), pp. 645-655.
[39] H.K.D.H. Bhadeshia, *Acta Metall.*, 1980, vol. 28(8), pp. 1103-1114.
[40] Y.C. Jung, Y. Ohomori, K. Nakai, H. Ohtsubo, *ISIJ Int.*, 1997, vol. 37(8), pp. 789-796.
[41] J.-Y. Yan, J. Ågren, J. Jeppsson, *Metall. Trans. A*, 2020, accepted.